5-2024

On-Demand Fabrication of Piezoelectric Sensors for In-Space Structural Health Monitoring

Amanda White
Boise State University

Isaac Little
Boise State University

Anastasiya Artyuk
Boise State University

Nicholas McKibben
Boise State University

Fereshteh Rajabi Kouchi
Boise State University

See next page for additional authors

OPEN ACCESS
IOP Publishing
Smart Materials and Structures
Smart Mater. Struct. **33** (2024) 055053 (16pp)
https://doi.org/10.1088/1361-665X/ad3d16

On-demand fabrication of piezoelectric sensors for in-space structural health monitoring

Amanda White[1], Isaac Little[1], Anastasiya Artyuk[1], Nicholas McKibben[2], Fereshteh Rajabi Kouchi[2], Claire Chen[3], David Estrada[2,4] and Zhangxian Deng[1,4,*]

[1] Department of Mechanical and Biomedical Engineering, Boise State University, Boise, ID 83725, United States of America
[2] Micron School of Materials Science and Engineering, Boise State University, Boise, ID 83725, United States of America
[3] Department of Chemical Engineering, University of Texas at Austin, Austin, TX, United States of America
[4] Center for Advanced Energy Studies (CAES), Idaho Falls, ID 83401, United States of America

E-mail: zhangxiandeng@boisestate.edu

Received 16 January 2024, revised 1 March 2024
Accepted for publication 10 April 2024
Published 26 April 2024

Abstract

Inflatable structures, promising for future deep space exploration missions, are vulnerable to damage from micrometeoroid and orbital debris impacts. Polyvinylidene fluoride-trifluoroethylene (PVDF-trFE) is a flexible, biocompatible, and chemical-resistant material capable of detecting impact forces due to its piezoelectric properties. This study used a state-of-the-art material extrusion system that has been validated for in-space manufacturing, to facilitate fast-prototyping of consistent and uniform PVDF-trFE films. By systematically investigating ink synthesis, printer settings, and post-processing conditions, this research established a comprehensive understanding of the process-structure-property relationship of printed PVDF-trFE. Consequently, this study consistently achieved the printing of PVDF-trFE films with a thickness of around 40 μm, accompanied by an impressive piezoelectric coefficient of up to 25 pC N^{-1}. Additionally, an all-printed dynamic force sensor, featuring a sensitivity of 1.18 V N^{-1}, was produced by mix printing commercial electrically-conductive silver inks with the customized PVDF-trFE inks. This pioneering on-demand fabrication technique for PVDF-trFE films empowers future astronauts to design and manufacture piezoelectric sensors while in space, thereby significantly enhancing the affordability and sustainability of deep space exploration missions.

Keywords: piezoelectric materials, in-space manufacturing, material extrusion, force sensor

* Author to whom any correspondence should be addressed.

1. Introduction

Inflatable re-entry vehicles and habitats are compelling for deep space exploration and the next-generation space station [1–5], due to their impressive volume-to-mass ratio and efficient packaging. Figure 1 shows a typical multi-layer inflatable habitat shell developed by NASA, which consists of an external thermal blanket, micrometeoroid orbital debris (MMOD) shielding, Kevlar restraint layer, and pressurized bladder layer.

The thin-walled inflatable structures are highly susceptible to damage from MMOD. Consequently, ensuring the sustainable and safe operation of these inflatable structures in future deep space exploration missions relies on the development of non-intrusive, convenient, and reliable structural health monitoring (SHM) technologies. Ideally, SHM sensors should have the ability to continuously detect the magnitude and impact location of MMOD forces around the clock while minimizing energy consumption. MMOD sensors are strategically positioned on the critical Kevlar restraint layer, the key component that bears the primary structural load and ensures structural integrity. Protected by external insulation layers, the Kevlar restraint layer is safeguarded against ionizing radiation and temperature variations, creating a stable environment that allows for the integration of traditional strain or force sensors, such as capacitive strain gauge, resistive strain gauge, piezoresistive strain guages, and optical fibers [6–13]. These sensors have demonstrated good accuracy and mechanical robustness. However, their utilization in inflatable structures is limited, either due to a continuous reliance on an external power source or the inadequate frequency bandwidth for detecting impact forces. A promising alternative is piezoelectric sensors, which typically comprise a piezoelectric layer sandwiched between a pair of electrodes [14]. When subjected to mechanical stimuli, electrical charges accumulate on the surface of the piezoelectric layer, resulting in a voltage across the electrodes. The voltage magnitude increases linearly with respect to the applied force magnitude. Previous studies have arranged multiple piezoelectric sensors in a two-dimensional grid, leading to the development of tactile sensor arrays capable of detecting both force magnitude and location [15, 16].

Piezoelectric materials are classified into three categories: single-crystals, polycrystalline piezoceramics, and polymers. Single-crystal piezoelectrics, such as aluminum nitride and lithium niobate, are noted for their suitability in high-temperature and radioactive conditions [17]. However, their piezoelectric response is relatively low, and existing in-space manufacturing techniques can hardly achieve the desired single-crystal structure. Piezoceramics, like lead zirconate titanate, offer the strongest piezoelectric response but are limited by their toxicity, making them unsuitable for applications in inflatable habitats. Innovations have led to the development of lead-free and biocompatible alternatives, such as barium titanate and bismuth titanate. Nonetheless, fabrication of piezoceramics requires high-temperature thermal sintering that exceeds the capabilities of current in-space manufacturing technologies, and their brittleness complicates integration onto flexible substrates.

Piezoelectric polymers offer an optimal balance between piezoelectric performance and flexibility. Among them, polyvinylidene fluoride (PVDF) and its copolymer with trifluoroethylene (PVDF-TrFE) stand out for their biocompatibility, chemical resistance, and notable piezoelectric properties. Specifically, PVDF-TrFE is more advantageous in in-space manufacturing due to its higher piezoelectric coefficient (25–30 pC N^{-1}) and its simpler processing requirements. Unlike PVDF, which necessitates the use of more volatile solvents and a complex combination of mechanical stretching and electrical poling to reach optimal piezoelectricity, PVDF-TrFE offers a more straightforward path to achieving desired piezoelectric properties. Table 1 provides an overview of conventional PVDF-trFE fabrication processes, which generate significant waste or necessitate additional subtractive machining to create complex customized designs.

Additive manufacturing of PVDF-trFE holds significant promise, offering an environmentally friendly and cost-effective approach to on-demand and rapid prototyping of complex piezoelectric sensor networks. Most previous additive manufacturing efforts have concentrated on piezoelectric composites, which incorporate piezoelectric ceramic particles within a passive or piezoelectric polymer matrix. While particle inclusion enhances piezoelectric response, it often compromises mechanical robustness and flexibility [22–24]. Particles can agglomerate or settle over time, limiting the shelf life of the ink. Table 2 presents a comparison of state-of-the-art additive manufacturing techniques for pure piezoelectric polymers. Previous studies have suggested that a PVDF-trFE film thickness in the range of 20–40 μm is ideal, as it is thin enough for convenient electrical poling and yet thick enough to yield a significant piezoelectric response [25, 26]. However, inkjet printers impose strict requirements on ink viscosity and solvent compatibility. Existing piezoelectric inks for inkjet printing typically contain only 0.8–1.2 wt.% PVDF-trFE, and more than 15 printing layers are required to achieve a thickness exceeding 20 μm.

Material extrusion (MEX) offers the capability to precisely deposit sub-nanoliter volumes of inks on flat or curved substrates and can accommodate inks with a wide viscosity range, from 1 cps (similar to water) to 1000 000 cps (similar to honey). Recent tests conducted during parabolic flights and aboard the International Space Station have confirmed the viability of MEX in a microgravity environment [34–37]. While MEX also offers the possibility of printing piezoelectric inks with higher concentrations of PVDF-trFE, thus expediting the fabrication process, a comprehensive study on the use of MEX for producing pure PVDF-trFE sensors has not yet been conducted.

This study thoroughly explores the MEX of PVDF-trFE devices. Our team delves into several critical aspects, encompassing ink formulation, printer configuration, and post-processing techniques. It places particular emphasis on a detailed examination of the drying process, curing

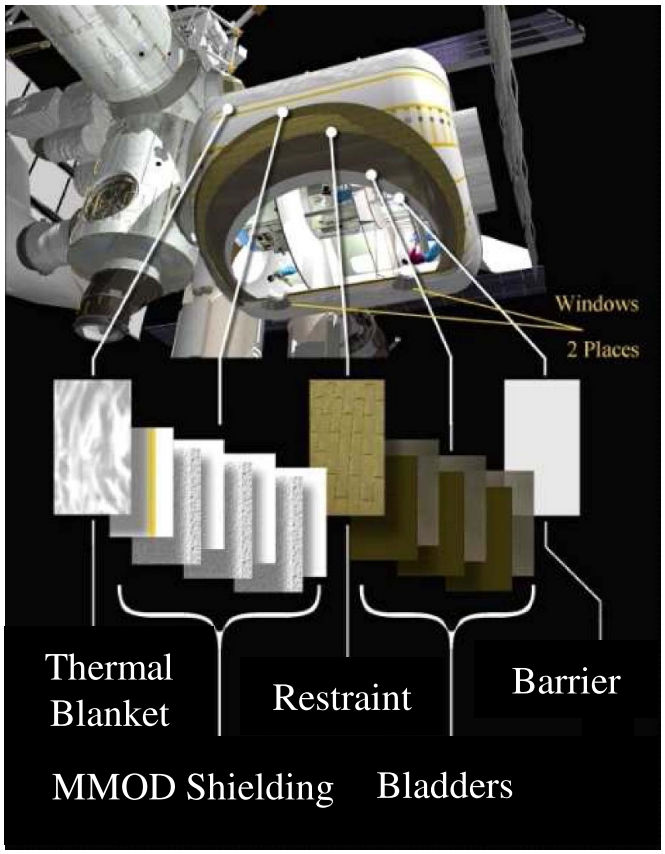

Figure 1. Cut-away view of NASA's TransHab inflatable habitat design.

methods, and fine-tuning of ink flow rates to achieve precise and uniform PVDF-trFE film thickness. Furthermore, the study explores multiple poling techniques, such as electric field poling and corona poling, to assess their effectiveness in PVDF-trFE polarization. Eventually, this study integrates commercial silver pastes with the newly formulated PVDF-trFE inks, resulting in an all-printed piezoelectric force sensor with an expanded frequency bandwidth.

2. Fabrication methods

2.1. Ink preparation

The performance of PVDF-trFE is sensitive to the ratio of vinylidene/trifluoroethylene (VDF/trFE). Commercially available PVDF-trFE powders exhibit a range of VDF/trFE ratios, spanning from 80:20 mol to 55:45 mol. It is observed that an increase in trFE mol.% leads to an elevation in the maximum dielectric constant of PVDF-trFE, and the dielectric constant peak occurs at a lower operating temperature [38]. Notably, PVDF-trFE with a trFE concentration of 20 mol.% attains the highest Curie temperature (136 °C) while maintaining a moderate piezoelectric coefficient (d_{33}) in the range of 24–30 pC N^{-1}. Consequently, this study utilized a commercial PVDF-trFE with 20 mol.% trFe (Piezotech FC20).

For MEX ink synthesis, this study started with two well-established recipes for inkjet printing [25, 26], employing a cosolvent system composed of methyl ethyl ketone (MEK, Macron Fine Chemicals) and dimethyl sulfoxide (DMSO, 99.9% Sigma Aldrich) in a 1:2 volume ratio. In this system, MEK serves as the primary solvent for PVDF-trFE, while DMSO slows down MEK evaporation at room temperature. Traditional inkjet inks typically contain 0.8–1.0 wt.% PVDF-trFE, necessitating time-consuming multilayer printing to achieve the desired thickness. Previous studies in our research group experimented with dissolving 5–20 wt.% of PVDF-trFE in the cosolvent system and established that inks with a 10 wt.% PVDF-trFE concentration yield the desired film thickness and uniformity [39], which was selected for this study. All ink components, including PVDF-trFE powders, DMSO, and MEK, were mixed within a glass vial using an analog vortex mixer (Fisherbrand) at 40% of the maximum speed (approximately 1200 rpm) for 1 h.

2.2. MEX

MEX in this study was carried out using a 2-axis nScrypt Microdispenser (150-3Dn-HP) situated within the Idaho Microfabrication Laboratory at Boise State University. NASA has recently conducted preliminary parabolic flight tests on a similar 5-axis nScrypt MEX system and has plans for its deployment to the International Space Station. This MEX system is compatible with inks spanning a viscosity range from that of water to honey (1 cps to 1 million cps), encompassing the viscosity of our PVDF-trFE ink.

The physical assembly and working principles of the nScrypt MEX system are depicted in figure 2. Compressed air serves as the driving force, propelling the ink through the valve. All O-rings used in the system are made of ethylene propylene diene monomer rubber, ensuring chemical compatibility with the ink. The printer head is vertically adjustable to achieve control over the gap between the nozzle and the substrate. In this study, a gap of approximately 0.2–0.3 mm was maintained to prevent the nozzle from touching the printed films while also mitigating ink overspray. The selected substrate is single-sided copper-coated Kapton (Shenyi SF305), consisting of a 50 μm thick polyimide layer coated with a 35 μm thick copper layer. The substrate was securely held in place by a vacuum chuck mounted on a motorized micro stage.

For a given combination of ink and substrate, the dimensions of the printed lines, including cross-sectional shape, width, and thickness, are determined by several factors. These include the contact angle between the ink droplet and the substrate, the ink flow rate through the nozzle, and the printing speed (v_s), which corresponds to the linear motion of the micro stage. Prior to printing, the substrate underwent a thorough cleaning process using isopropyl alcohol (IPA), followed by

Table 1. Conventional fabrication methods for commercial PVDF-trFE sensors.

Method	Merit	Drawback
Solvent casting [18]	· Convenient	· Cannot form complex geometries · Difficulty in thickness control · High batch-to-batch variation
Screen printing [19]	· Can form complex geometries · Easy multilayer printing	· Large waste production · Relatively low precision · High batch-to-batch variation · Must work quickly to prevent drying/sticking · Cleaning required between each printed layer
Spin coating [20, 21]	· Good film uniformity · Easy thickness tuning	· Large waste production · Complex designs require photolithography

Table 2. State-of-the-art additive manufacturing techniques for PVDF-trFE fabrication.

Method	Merit	Drawback
Fused filament printing [27, 28]	· Easy filament extrusion · Potential *in-situ* post-processing	· Poor thin film printing quality · Poor film adhesion · Difficulty in electrode fabrication
Electrospinning [29, 30]	· No post-processing needed · Generate nano- or micro-fibers	· Produce high porosity and low mechanical strength structures
Inkjet printing [25, 31–33]	· Convenient · Simultaneous electrode printing	· Cannot print high viscous inks · Ink may dry and clog the cartridge · Time-consuming

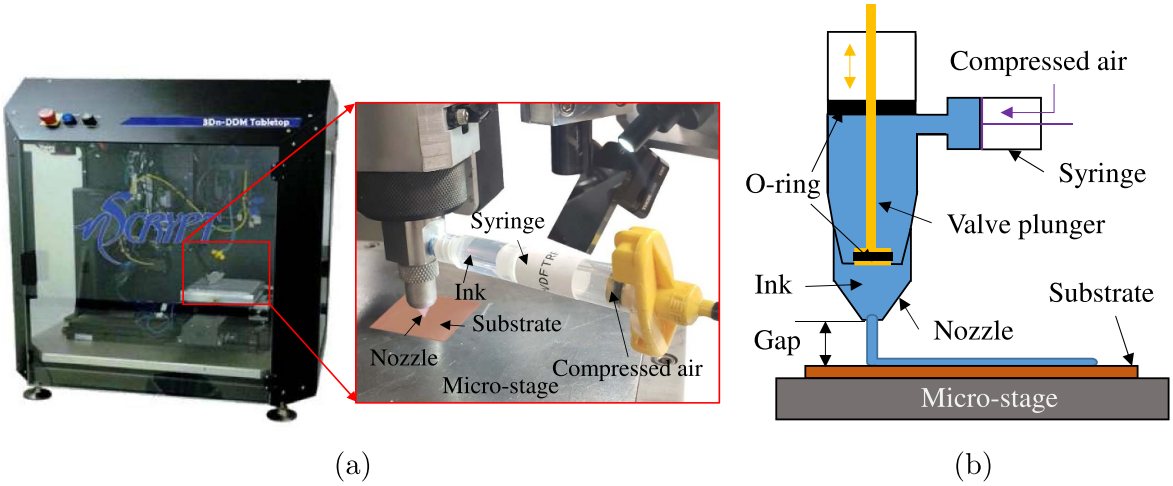

Figure 2. The nScrypt 150-3Dn-HP material extrusion system: (a) physical assembly and (b) schematic.

blow-drying with compressed nitrogen gas. This chemical surface treatment effectively removes any contaminants from the substrate, enhancing the ink's wettability and reducing its contact angle on the substrate. The ink flow rate, on the other hand, relies on various parameters, such as the valve aperture (ΔV), which represents the vertical displacement of the valve plunger, and the compressed air pressure (P). The individual effects of v_s, ΔV, and P are further explored and discussed in subsequent sections.

2.3. Curing

The curing process for as-printed PVDF-trFE involves two essential stages: first, the removal of the MEK:DMSO co-solvent through drying, and second, the cross-linking or crystallization of PVDF-trFE polymers. Without a proper curing process, PVDF-trFE films may exhibit undesirable characteristics, such as visible bubbling, the coffee ring effect, or film delamination, as illustrated in figure 3. The efficiency of the

Figure 3. Unsuccessful curing of 10 × 10 mm printed PVDF-trFE films: bubbling (left) and coffee ring effect (right).

curing process depends on both temperature and duration and requires further optimization.

2.4. Poling

The piezoelectricity in PVDF-trFE originates from its crystalline structures. As-cured PVDF-trFE films primarily contain the α- and β-phases. The α-phase is nonpolar, resulting in randomly-oriented dipoles and insignificant piezoelectric responses. Conversely, the β-phase exhibits a trans planar zigzag configuration, leading to strong polarization or piezoelectric responses. However, the α-phase predominates in as-cured PVDF-trFE films as it represents the thermodynamic ground state with the lowest energy. Poling, or using an external electric field to reorient the dipoles, is an effective process for transforming the α-phase into the β-phase, thereby enhancing the material's piezoelectric characteristics. This study investigates three distinct poling techniques, each with its own approach to applying an electric field across the sample. The specific setups for these techniques are illustrated in figures 4–6.

Electric field poling—oil bath. Previous studies have demonstrated that the application of either a DC voltage or a low-frequency AC voltage to create a uniform electric field across the PVDF-trFE film is an efficient method for achieving poling [19]. Using a dedicated commercial fixture (PolyK Technologies), this study exclusively focuses on DC voltage due to its simplicity and ability to maintain stable polarization. As depicted in figure 4, the top pin of the fixture is connected to a high-voltage power supply (Trek 610E), while the bottom is grounded. An additional stainless steel shim is used to ground the copper coating on Kapton. To prevent corona discharge and minimize temperature gradients within the PVDF-trFE film, the film is fully immersed in dielectric silicone oil (Grainger, ISO viscosity grade 100, SAE grade 80W, and H1 food grade).

Electric field poling—tungsten needle. The oil bath rig necessitates the deposition of a top electrode on the PVDF-trFE film prior to poling. The use of a silicone oil bath in electric field poling can also introduce contamination to the sample surface, presenting challenges, especially in critical fields like biomedicine and the food industry. Moreover, poling thick films or large samples demands high voltage and current, which might exceed the capabilities of standard commercial power supplies. To resolve these challenges, this study introduces an alternative poling method, as shown in figure 5. This method uses the electric field magnification effect, enabling the generation of a high electric field in the vicinity of a sharp needle. While this particular poling setup is less commonly utilized in PVDF-trFE fabrication, it holds practical value for *in-situ* poling in fused filament fabrication [28, 40], where a DC electrical field is applied to the sharp printer nozzle. In this configuration, the sample was affixed to a micro-stage, allowing precise adjustment of the relative position between the sample and the tungsten needle (McCrone Group #2 sharp). A DC voltage was applied to the needle, positioned at a distance of 0.1 mm from the cured PVDF-trFE film.

Corona poling. Both electric field poling approaches impose strict demands on film uniformity since any thin areas caused by bubbling or the coffee ring effect can result in an excessive electrical field strength across the film, potentially leading to film breakdown. The electric field magnification effect, in particular, can only achieve PVDF-trFE poling over a small region. To tackle these challenge, our team explored the corona poling approach [27, 41, 42]. Corona poling works by applying a high voltage to a sharp electrode, generating a corona discharge that creates a strong, non-uniform electric field, which reorients the piezoelectric dipoles. Figure 6 illustrates our corona poling rig modified from the electric field poling rig. To enable precise temperature control within the PVDF-trFE films, a thermoelectric plate (BXQINLENX TEC1-12710) was added atop the steel plate. Temperature regulation was accomplished through an open-loop controller, where the correlation between the current applied to the thermoelectric plate and the corresponding temperature of the plate was calibrated using an infrared thermal camera (Fluke 62). The corona discharge from the tungsten needle was enclosed within a polylactic acid (PLA) tube with a diameter of 6.35 mm. The dimensions of the PLA tube can be adjusted to accommodate various sample sizes.

3. Characterization methods

3.1. Profilometry

A stylus profilometer (Bruker Dektax XT-A) was employed to characterize the thickness of the MEX-printed PVDF-trFE. The stylus tip had a diameter of 25 μm, and a consistent contact force of 5 mg was applied. To accurately replicate three-dimensional surface topography, we set the horizontal and vertical scanning resolutions at 2.166 μm and 65 μm, respectively. The flexible Kapton substrate coated with copper was prone to wrinkling, which resulted in inaccuracies in the surface topography measurements. To address this issue, a 200 nm thick copper coating was sputtered on a silicon wafer with a diameter of 100 mm and a thickness of 500 μm (University Wafer Inc. ID 590). This copper-coated wafer effectively simulated the copper/PVDF-trFE interaction while ensuring a perfectly flat surface for profilometry.

3.2. Differential scanning calorimetry and thermogravimetric analysis

The investigation covered the dynamic behaviors of the air-drying process for the MEK:DMSO cosolvent system and the

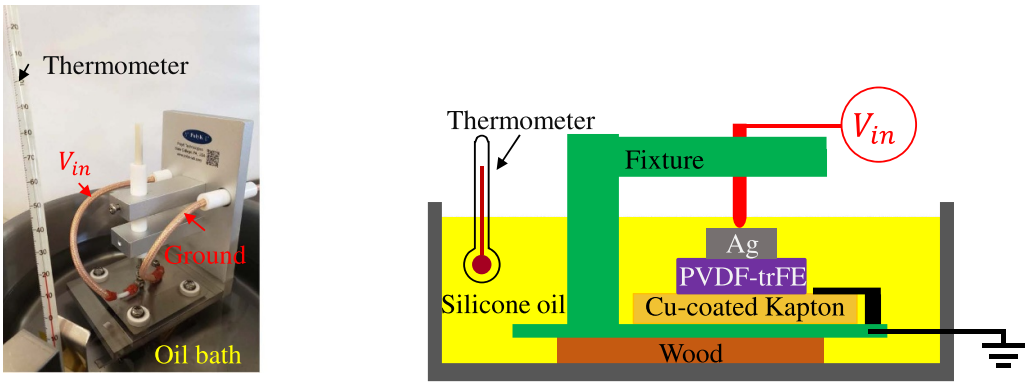

Figure 4. Electric field poling rig submerged in a silicone oil bath: (a) physical assembly and (b) schematic.

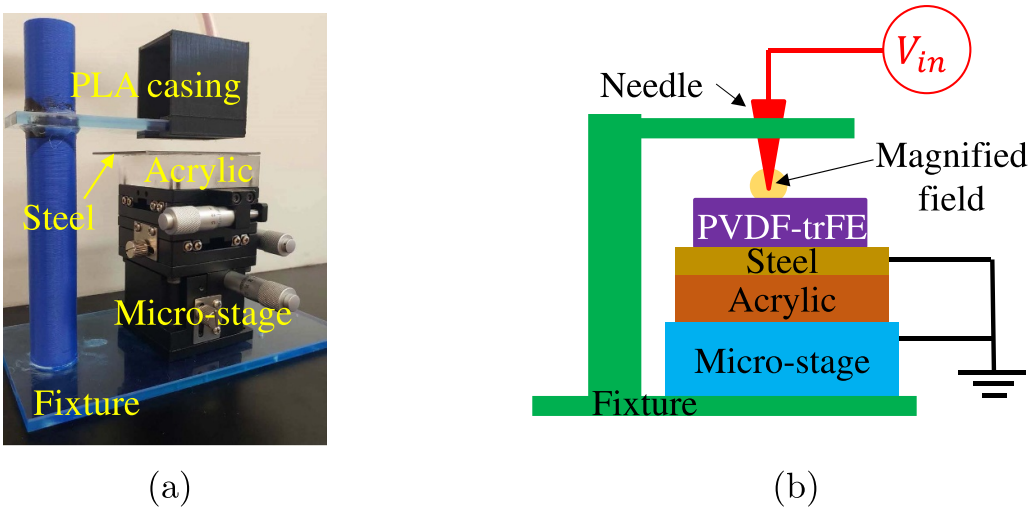

Figure 5. Electric field poling rig facilitated by a magnified electric field around a tungsten needle: (a) physical assembly and (b) schematic.

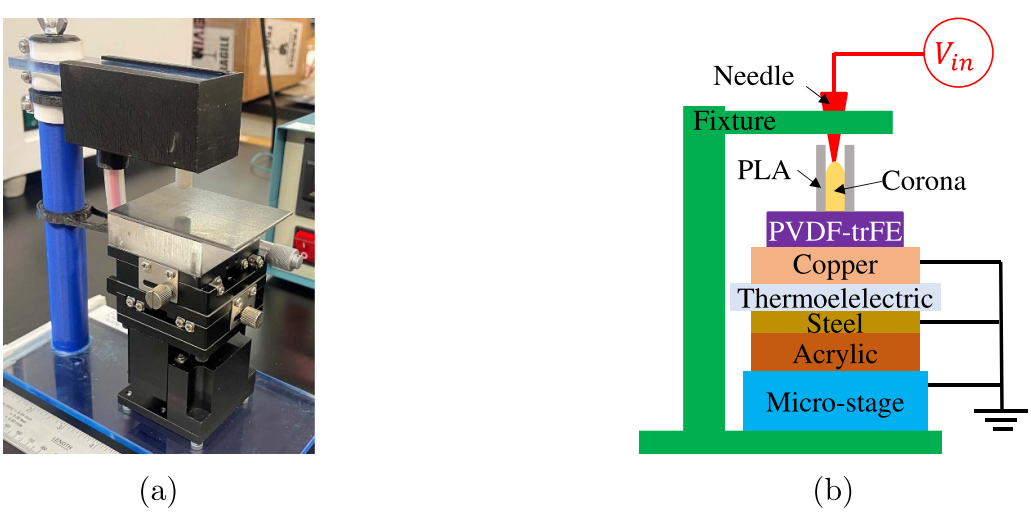

Figure 6. Corona poling rig: (a) physical assembly and (b) schematic.

thermal characteristics of PVDF-trFE powder using a thermogravimetric analysis–differential scanning calorimetry (TGA-DSC) instrument (Netzsch STA 449 F5 Jupiter). Alumina crucibles were utilized to hold the samples. The air-drying process was examined at room temperature (25 °C). For the PVDF-trFE powder characterization, the temperature

increased from 20 °C to 160 °C at a heating rate of 5 °C min^{-1}. All measurements were conducted under an airflow rate of 20 ml min^{-1}.

3.3. Surface contact angle

Contact angle analysis plays a pivotal role in MEX by providing critical insights into ink-substrate interactions. These measurements offer valuable information about ink wettability, which directly influences the ability of the ink to spread and adhere uniformly to the printing surface. Contact angle measurements were conducted using an optical tensiometer (Biolin Scientific Theta). To determine the contact angle of the synthesized ink on a copper substrate, the sessile drop technique was employed, and calculations were based on the classical Young–Laplace equation. Contact angle measurements were carried out at various temperatures.

For the room-temperature (25 °C) measurement, a 10 μl droplet of ink was deposited onto a 20 × 20 mm copper substrate, and changes in the contact angle were recorded over a 6 h period in an open-air environment. In contrast, for measurements at elevated temperatures, a 20 × 20 mm copper substrate was placed on the hot side of a thermoelectric plate (Peltier) and secured with Kapton tape, as depicted in figure 7. This prepared substrate was then positioned on the tensiometer's stage. The current supplied to the thermoelectric plate was regulated using a current-limiting benchtop linear power supply (CSI1802X, Circuit Specialists), and the resulting plate temperature was monitored using a thermal imaging camera (Keysight U5855A). A 10 μl droplet of the ink was deposited onto the heated copper substrate, and changes in contact angles were recorded until the droplet completely evaporated at each of the specified temperatures (50 °C, 90 °C, and 110 °C).

3.4. Piezoelectric coefficient

The effectiveness of electric field poling was evaluated using the piezoelectric coefficient d_{33}, which describes the amount of electrical charges accumulated on the PVDF-trFE film per unit compressive force applied norm to its surface. The measurement involved applying a dynamic force of approximately 0.25 N at 110 Hz, accompanied by a DC compression force of around 2.5 N to the PVDF-trFE film. Under the influence of dynamic force excitation, the PVDF-trFE accumulated positive charges on one side (anode) and negative charges on the other side (cathode). Depending on the orientation of the PVDF-trFE films relative to the d33 meter probes, the resulting d_{33} value could be either positive, denoted as d_{33}^{p}, or negative, denoted as d_{33}^{n}. To obtain the final d_{33} value, both positive and negative d_{33} measurements were conducted for each sample by flipping the samples over, and the average value was calculated as $d_{33} = (d_{33}^{p} - d_{33}^{n})/2$. This approach effectively mitigated any potential drift in the d33 meter. To ensure accurate measurements of d_{33}, all samples were peeled off from the Copper-coated Kapton due to the dielectric nature of the Kapton layer.

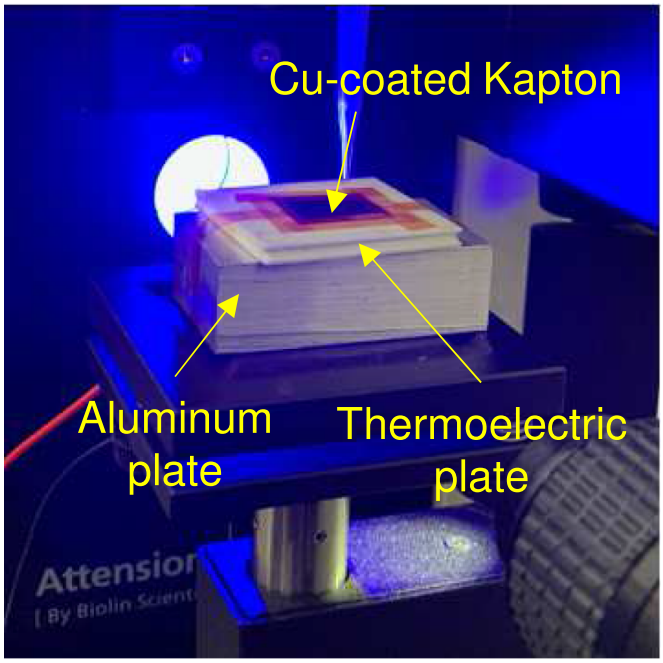

Figure 7. Experimental setup to characterize droplet contact angle at high temperatures.

Table 3. Printer parameters selected based on iterative experimentation.

Printer Parameter	Value
Nozzle diameter	300 μm
Air pressure P	68.95 kPa
Printing speed v_s	6 mm s^{-1}
Valve aperture ΔV	0.04 mm
Line spacing	0.3 mm

4. Fabrication optimization

4.1. Printer parameters

Our prior experience with MEX highlighted the critical role of three key parameters in controlling the dimensions and geometries of the printed PVDF-trFE: compressive air pressure (P), valve opening (ΔV), and printing speed (v_s). The value of v_s is determined by the linear speed of the micro-stage. Based on practical experience and the manufacturer's recommendations, a minimum increment for P, ΔV, and v_s was established at 0.689 kPa, 5 μm, and 0.5 mm s^{-1}, respectively. An optimal set of printer parameters that consistently produced approximately 40 μm thick PVDF-trFE films on copper-coated Kapton was determined through iterative experiments. The resulting parameters are summarized in table 3. Subsequently, the printed PVDF-trFE films were transferred to a preheated oven set at 90 °C and cured for 15 min. Further discussion on the curing conditions will be presented in subsequent sections.

For precise control over the geometry of the printed PVDF-trFE films, this study conducted a detailed exploration of the effects of varying P, ΔV, and v_s within proximity of their nominal values, as presented in table 3. Specifically, the pressure

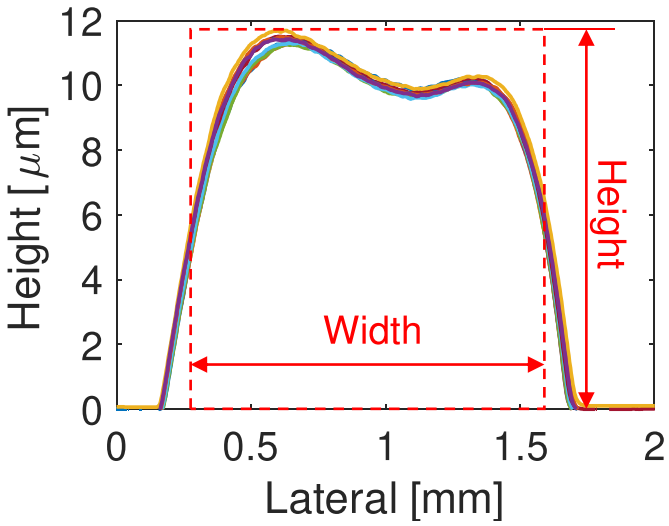

Figure 8. A total of 10 cross sections of the printed PVDF-trFE lines plotted on top of each other.

ranged from 41.37 kPa to 96.53 kPa, incremented in 13.79 kPa intervals; the printing speed spanned from 2 to 10 mm s^{-1}, incremented in 2 mm s^{-1} steps; and ΔV ranged from 0.30 μm to 50 μm, incremented in 5 μm increments. During these experiments, one of these settings was systematically varied within the specified range, while the other two settings were held constant at their nominal values.

For each unique printer configuration, a 10 mm long line was printed on copper-coated silicon wafers treated with IPA. The printer was allowed to stabilize for a few minutes before initiating the print. Subsequently, the cross-sectional profiles of the printed lines at 10 distinct locations, each 1 mm apart, were characterized. Figure 8 illustrates the cross-sectional profiles obtained using stylus profilometry.

Notably, the quality of the printed lines remained consistent, with no discernible variations observed across the 10 cross sections. The height of the line, labeled as H, was determined at its maximum point, and the width, denoted as W, was measured as the distance between points where the height reached half of its maximum value. The cross-sectional area, represented as V_n, quantifies the size of the printed lines and can be estimated as follows:

$$V_n = \frac{Q}{v_s}. \tag{1}$$

Here, Q is the ink flow rate through the printer nozzle and

$$Q = C_f \Delta V \sqrt{\frac{2(P - P_0)}{\rho}}, \tag{2}$$

where C_f is a constant related to the orifice dimensions and Reynold's number, P_0 is the pressure outside of the nozzle, and ρ is the ink density.

Based on equations (1) and (2), the assumption is made that the cross-sectional area V_n can be described by the following equation (equation (3)), which incorporates additional parameters k_4 and k_5 to account for variations in the valve aperture and micro-stage motion:

$$V_n = \frac{k_1 \Delta V \sqrt{k_2 P + k_3} + k_4}{v_s} + k_5. \tag{3}$$

The results presented in figure 9 confirm the accuracy of equation (3) in predicting V_n. Eventually, the following parameter values provided an excellent fit: $k_1 = 26.61$, $k_2 = 340.87$, $k_3 = 7977.94$, $k_4 = -122.06$, and $k_5 = 1.04$. Any of the three selected parameters can be adjusted to achieve the desired V_n. However, it is recommended to use the valve opening ΔV as the primary printer setting, as V_n exhibits a linear relationship with respect to it. This approach simplifies the process for future users, who can perform surface profilometry for two different ΔV settings to accurately predict V_n.

The shape of the cross-section is influenced by the surface contact angle between the droplet and the substrate. Consequently, for a given ink/substrate combination with a fixed wettability, the values of W and H are uniquely determined by V_n. The relationship between H and W with respect to the cross-sectional area V_n is established based on profilometry data collected from all 15 printer settings, as depicted in figure 10. This result confirms that the values of H and W are determined by the total ink volume deposited on the substrate, regardless of how the ink volume was controlled. In other words, achieving the target W and H is possible using P, ΔV, or v_s, as long as the same V_n is achieved. We have successfully achieved consistent printing of PVDF-trFE lines with a width as narrow as 0.75 μm.

4.2. Curing

The DSC curve obtained from pure PVDF-trFE powders, as depicted in figure 11, displays two distinct endothermic peaks. The first peak, observed at 113 °C, corresponds to the Curie temperature (T_c), signifying the transition from the ferroelectric phase to the paraelectric phase. The second peak, occurring at 147 °C, aligns with the melting point (T_m) of PVDF-trFE. It is worth noting that PVDF-trFE crystallizes in the paraelectric phase within the temperature range between T_c and T_m.

To ensure the complete polymer crosslinking and crystallization, all printed PVDF-trFE films underwent a thermal annealing process at 130 °C for a duration of 1 h in a mechanical oven (Thermo Scientific Heratherm General Protocol). This annealing condition is recommended by the vendor. Subsequently, the samples were allowed to cool gradually inside the oven, a procedure aimed at eliminating the potential for thermal shocks that could compromise the integrity of the film/substrate interface.

The PVDF-trFE inks as printed include solvents, and the literature provides several approaches for solvent removal. For instance, Haque et al. proposed a two-step process in which PVDF-trFE dissolved in MEK:DMSO was initially subjected to room temperature air drying with a constant airflow for

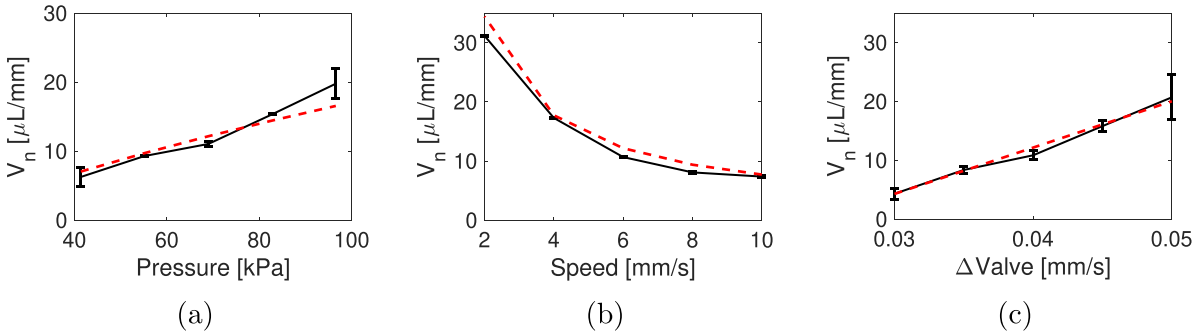

Figure 9. The value of V_n under varying (a) pressure P, (b) printing speed v_s, and (c) ΔV. The solid black lines denote experimental results and the red dashed lines denote simulation results.

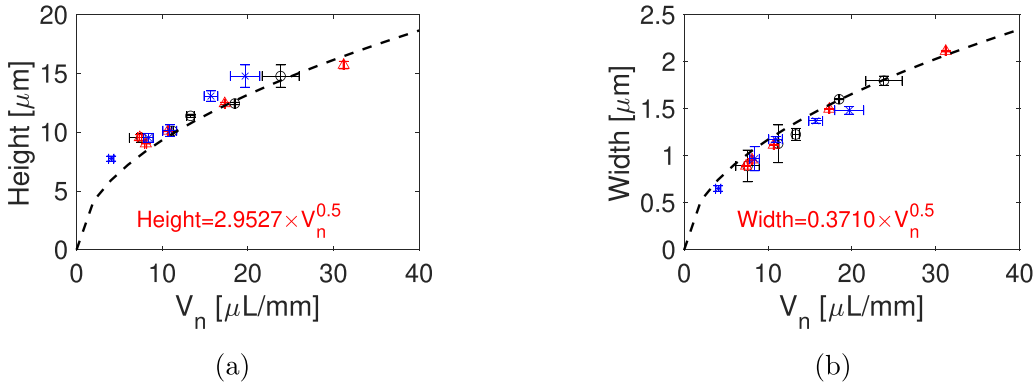

Figure 10. The dimensions of the printed PVDF-trFE lines using different printer settings: (a) height H and (b) width W.

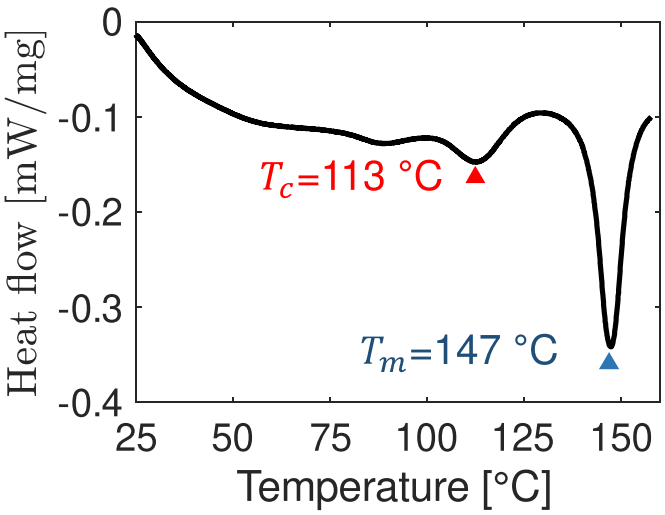

Figure 11. The heat flow measurement of pure PVDF-trFE powders from 25 °C to 160 °C.

24 h, allowing for the gradual removal of MEK. Subsequently, the air-dried droplets underwent a 30 min heating step in an oven at 90 °C to completely evaporate the DMSO [25]. In contrast, Thuau et al. combined cosolvent drying with polymer annealing by directly placing the PVDF-trFE droplets, dissolved in a Cyclopentanone:DMSO cosolvent, on a hot plate at 140 °C for 1 h [26]. However, none of these studies provided a quantitative assessment of how drying temperature and duration affect the final film quality.

To comprehensively assess the viability of room temperature air drying while optimizing the sample preparation process, we dispensed PVDF-trFE ink droplets (approximately 15 μl each) onto IPA-treated copper-coated Kapton substrates using an Eppendorf pipette. This precise dispensing method yielded wet PVDF-trFE ink droplets with a diameter of roughly 5 mm, mirroring those produced through MEX. An investigation into the efficacy of air drying at room temperature (25 °C) was conducted by subjecting a group of these droplets to a mechanical oven equipped with continuous airflow. The drying process spanned various durations, ranging from 0 h to 24 h, with increments of 4 h. After air drying, the dried droplets were cured at 130 °C for 15 min in the same oven. The resulting PVDF-trFE films are depicted in figure 12. Drying the film for a short duration ($\leqslant$12 h) resulted in film shrinkage, whereas medium-duration air drying (12–20 h) led to a severe coffee ring effect. Further extending the air drying duration beyond 20 h caused film delamination.

Gaining insight into the air drying process, further analysis focused on weight loss and contact angle changes over time for the PVDF-trFE ink at room temperature, as depicted in figure 13. The weight loss curve reveals two distinct phases:

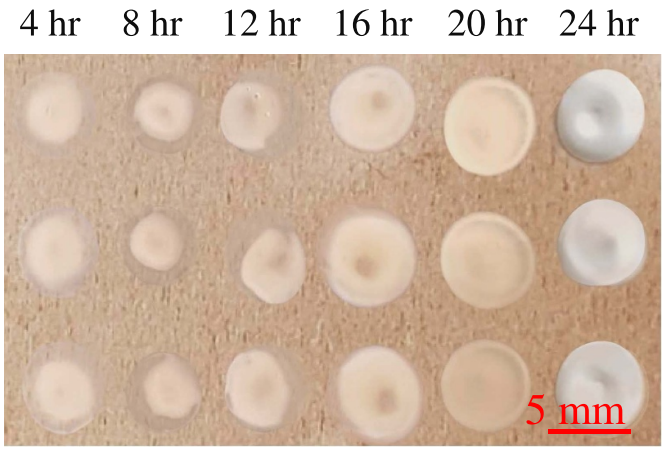

Figure 12. Optical images of air dried PVDF-trFE film.

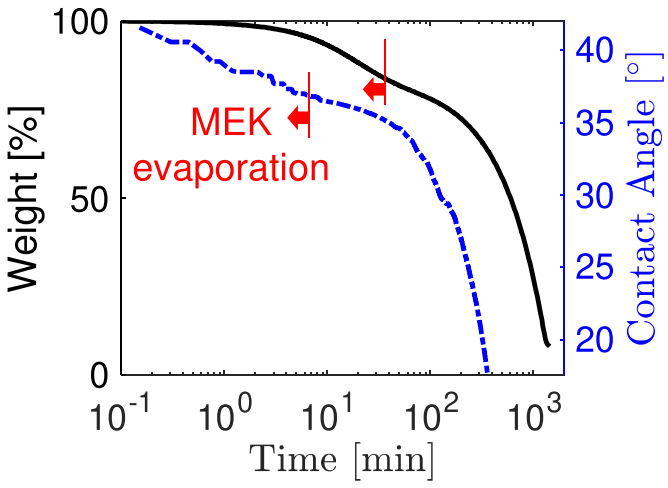

Figure 13. The thermogravimetric analysis result of PVDF-trFE ink at room temperature and surface angle of PVDF-trFE ink deposited on copper.

an initial rapid evaporation of MEK followed by a slower evaporation of DMSO. Similarly, the contact angle measurements exhibit a similar trend, with the rapid evaporation of MEK leading to a sharp reduction in the contact angle. The faster completion of MEK evaporation in the thermogravimetric analysis can be attributed to the relatively small droplet size, and it should be noted that MEK evaporation had already commenced during the sample preparation phase. These results underscore the reliability of surface contact angle measurements as indicators of solvent evaporation or changes in droplet composition.

Based on the experimental observations presented in figures 12 and 13, it is evident that short-duration air drying ($\leqslant$12 h) is insufficient for the complete removal of MEK during the initial stages of the drying process. As high-temperature annealing begins, the residual MEK leads to the migration of PVDF-trFE towards the center of the droplet, saturating the MEK and halting further movement. Consequently, short-period air drying results in a shrunk PVDF-trFE disc. Shrinkage of the PVDF-trFE film ceases for air drying durations exceeding 12 h. In such cases, all MEK within the droplet has evaporated, and the PVDF-trFE exists as particle suspensions in a pure DMSO system before the annealing process. During annealing, complex Marangoni flows occur, resulting in a pronounced coffee ring effect. Excessively long-duration air drying (24 h or more) removes both MEK and most of the DMSO from the droplet. Consequently, PVDF-trFE powders scatter on the substrate before annealing, mitigating the coffee ring effect. However, annealing fully dried PVDF-trFE leads to poor adhesion between the film and substrate, causing all samples to detach from the copper-coated Kapton tape after annealing. These results collectively suggest that air drying is not recommended for the curing of PVDF-trFE.

Furthermore, these results indicate that the ideal drying condition involves the simultaneous rapid evaporation of MEK and DMSO. Rapid evaporation prevents printed structure shrinkage, while simultaneous evaporation mitigates the coffee ring effect. To determine the optimal drying condition, particularly the drying temperature, contact angles were measured at temperatures of 50, 90, and 110 °C, as illustrated in figure 14. During air drying at 50 °C, two separate MEK and DMSO evaporation phases were observed. However, at both 90 °C and 110 °C drying temperatures, the contact angle exhibited a linear reduction over time, indicating simultaneously evaporation of MEK and DMSO.

Contact angle measurements beyond 110 °C were not feasible due to equipment limitations. Therefore, air drying at temperatures above 110 °C was conducted through a trial-and-error approach. Three additional PVDF-trFE droplets were printed using the MEX system and immediately subjected to drying for 15 min in a mechanical oven preheated to 90, 130, and 170 °C. Preheating the oven proved crucial to prevent MEK evaporation before the oven reached a steady state. The surface topography of PVDF-trFE films processed at different temperatures is presented in figure 15.

Drying the as-printed PVDF-trFE ink at 90 °C yielded superior film uniformity, while drying at 130 °C resulted in an uneven film surface with film shrinkage and distortion. Film shrinkage disappeared when the droplet was dried at 170 °C, and reasonable film uniformity was achieved. We hypothesize that this outcome is attributed to the boiling of MEK, as the boiling points of MEK and DMSO are 80 °C and 189 °C, respectively. At 90 °C, MEK slowly evaporated from the cosolvent system. At 130 °C, nucleate boiling or transition boiling occurred, leading to violent bubbling or explosive evaporation of MEK. As the temperature continued to rise, larger bubbles formed due to MEK evaporation, which could cause uneven films but did not alter the dimensions of the film.

To investigate the impact of drying duration on film quality, another set of MEX-printed PVDF-trFE droplets were dried at 90 °C for 15 min, 30 min, and 60 min. Interestingly, no significant differences were observed. This suggests that a

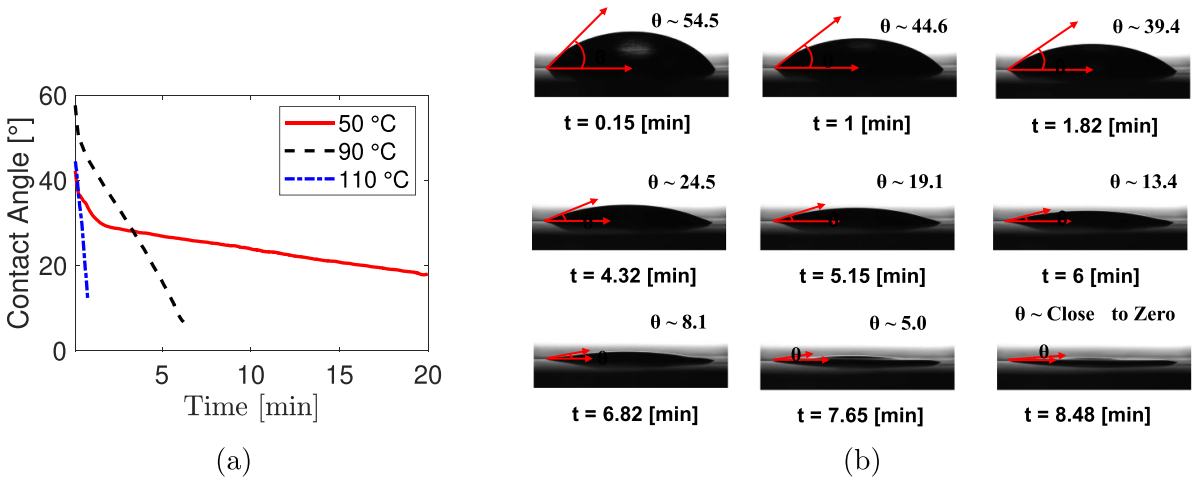

Figure 14. (a) Contact angle between ink droplets and copper at various temperatures and (b) droplet morphology change at 90 °C.

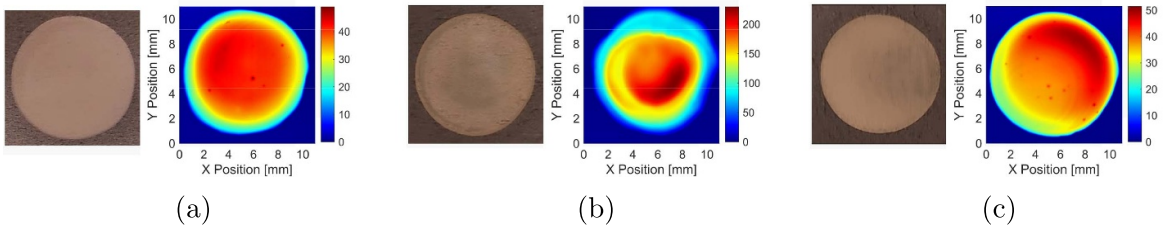

Figure 15. MEX-printed and 10 mm diameter PVDF-trFE films after curing for 15 min at (a) 90 °C, (b) 130 °C, and (c) 170 °C.

15 min drying duration is sufficient to completely remove the cosolvent, likely due to the small droplet size.

4.3. Electric field poling—oil bath

Electric field strength, temperature, and poling duration all play crucial roles in the electrical poling process, as indicated by previous studies [43]. Therefore, these parameters were systematically investigated in this study. Figure 16 illustrates the samples employed for electric field poling in a silicone oil bath. These samples consist of PVDF-trFE films printed on copper-coated Kapton substrates, each with a 10 mm diameter. Additionally, three 3 mm diameter silver dots, spaced approximately 5 mm apart, were printed onto the PVDF-trFE film. This arrangement allowed for the execution of three poling tests using a single sample.

The DC voltage applied across the film varied between 4 kV and 8 kV, with increments of 1 kV. These voltage settings resulted in an electrical field ranging from approximately 100 MV m^{-1} to 200 MV m^{-1}, based on the surface topography depicted in figure 15(a). As the temperature increases, PVDF-trFE softens and exhibits increased molecular mobility. However, exceeding the Curie temperature leads to a complete loss of piezoelectric response. In this study, the poling temperature was set in the range of 20 °C–60 °C, with 20 °C increments. Additionally, the poling durations (5, 10, and 30 min) were selected based on common practices in previous studies [43]. Figure 17 presents the d_{33} measurements obtained under different poling conditions. For each

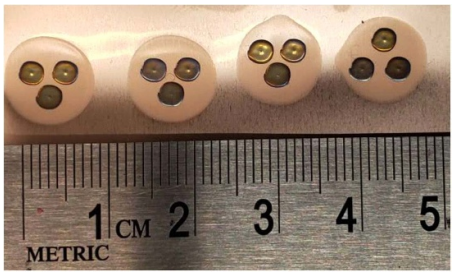

Figure 16. Dried and annealed PVDF-trFE films sandwiched between copper-coated Kapton and MEX-printed silver paste used for electrical poling optimization.

condition, a total of 5 samples were fabricated and characterized to account for uncertainties in the electrical poling process.

For the same duration and ambient temperature, the d_{33} value exhibits a gradual increase with respect to the applied voltage or electrical field strength across the PVDF-trFE. Due to the thickness variation in the printed PVDF-trFE films, a low poling voltage may not generate high enough electric field in certain regions, resulting in larger variations in d_{33}. A higher poling voltage ensures a sufficient electrical field even at locations where the thickness exceeds the average value. The effectiveness of electrical poling also increases as the poling temperature rises, particularly when the poling electrical field is low. As temperature increases, the variation in electrical poling also gradually diminishes. The impact of temperature

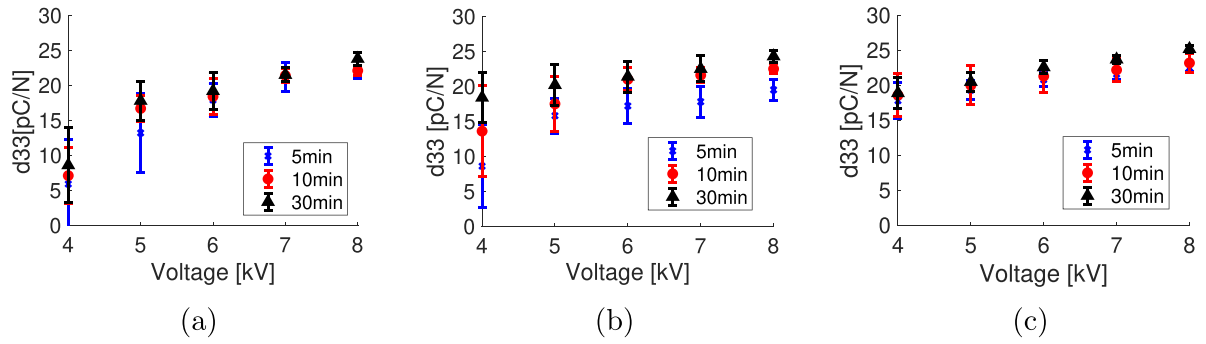

Figure 17. The d_{33} values of MEX-printed PVDF-trFE samples poled at (a) 20 °C, (b) 40 °C, and (c) 60 °C.

becomes negligible when the poling voltage reaches 8 kV or the poling electrical field is around 200 MV m^{-1}.

In cases involving a 30 min poling duration, a consistently higher d_{33} value is typically obtained at the same poling voltage and temperature. However, the influence of poling duration becomes negligible under conditions of high voltage or elevated temperature. Overall, the maximum d_{33} achieved was 25 ± 1 pC N^{-1}, obtained when the PVDF-trFE sample was poled at approximately 200 MV m^{-1} and 60 °C for 30 min, falling within the lower end of the nominal d_{33} range suggested by the vendor (25–30 pC N^{-1}). The PVDF-trFE film had thin layers of dielectric silicone oil covering it, which could not be fully removed prior to testing, possibly contributing to the observed reduction in the effective d_{33}.

4.4. Electric field poling—tungsten needle

To verify the effectiveness of the electric field poling mechanism facilitated by the electric field magnification near a tungsten needle, an additional set of 5 mm diameter PVDF-trFE discs were fabricated on IPA-treated 0.635 mm thick rigid copper plates. The electrical voltage applied to the tungsten needle was manually adjusted to maintain a poling current within the range of 20–30 μA. Beyond this range, the dielectric PVDF-trFE material may break down. Poling durations varied from 3 min to 17 min. The resulting piezoelectric coefficient d_{33} is displayed in figure 18, plotted against the poling current and duration.

The d_{33} value typically exhibits an increase with higher poling current or longer poling duration, although there was notable variability in the observed d_{33} values. In this preliminary test, the maximum d_{33} achieved was 20.5 pC N^{-1}. Though this value is approximately 7% lower than that obtained through room-temperature electric field poling in the silicone oil bath, the result confirms the feasibility of achieving electric field poling without the need for top electrodes. Future investigations may consider methods to enhance d_{33}, such as by heating the PVDF-trFE film or extending the poling duration.

4.5. Corona poling

The DC voltage V_p applied to the tungsten needle in the corona poling rig ranged from 17 kV to 23 kV, with 1 kV increments.

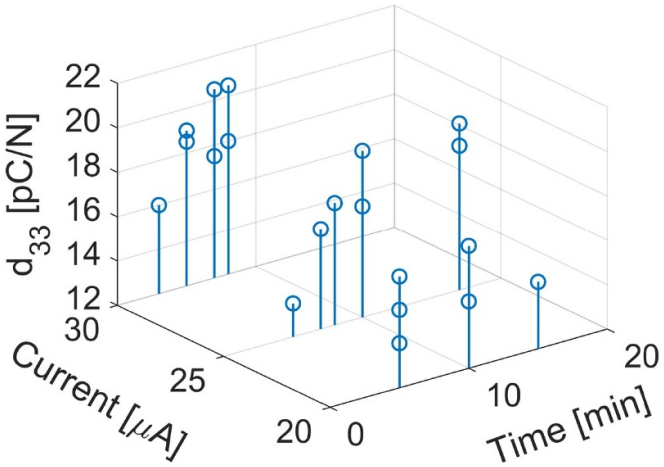

Figure 18. The resulting piezoelectric coefficient d_{33} under different electric field poling using a tungsten needle at room temperature.

Given the greater tolerance of corona poling to film thickness variation, the maximum poling temperature reached was 80 °C. Since the dielectric constant of PVDF-trFE decreases with increasing temperature, lower values of V_p were required to achieve the same corona strength at elevated temperatures. Using the same PVDF-trFE samples, the effect of poling duration t_p was studied, with durations set at 1 min, 3 min, 5 min, 10 min, 15 min, and 20 min for a given V_p and temperature. The d_{33} value was characterized once the PVDF-trFE film had completely cooled down to room temperature. Subsequent poling cycles were initiated only after the sample had been placed on the thermoelectric plate for at least 10 min to allow it to reach thermal equilibrium. The resulting piezoelectric coefficient d_{33} is displayed in figure 19, plotted against the DC voltage and poling duration.

The maximum d_{33} achieved was 21.1 pC N^{-1} at a temperature of 20 °C, V_p of 23 kV, and a poling duration t_p of 20 min. In general, for a fixed poling voltage and duration, higher temperatures enhance the mobility of PVDF-trFE polymers, resulting in a higher d_{33}. Additionally, the piezoelectric coefficient tends to increase as the poling duration t_p increases. However, the effect of further increasing t_p becomes negligible once it reaches a critical value. This critical value increases as the poling temperature rises, suggesting that high-temperature corona

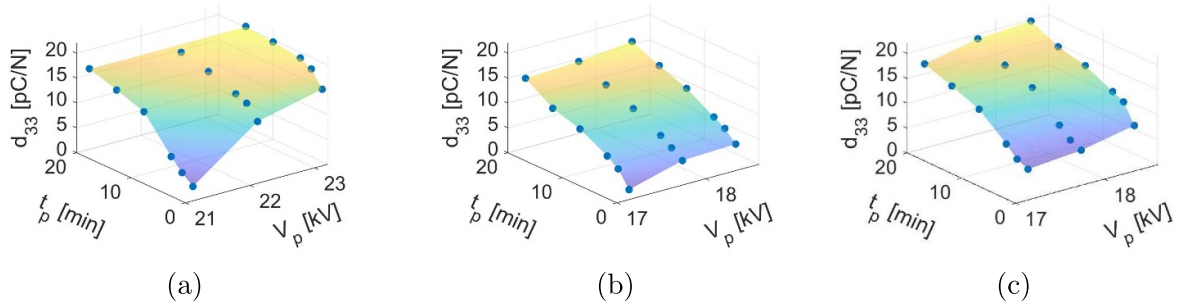

Figure 19. The d_{33} values of MEX-printed PVDF-trFE samples polarized using the corona poling setup at (a) 20 °C, (b) 60 °C, and (c) 80 °C.

poling beyond 20 min could potentially yield even higher values of d_{33}.

5. Device prototyping

A standard piezoelectric dynamic force sensor typically comprises a piezoelectric layer positioned between two electrodes. When subjected to stress, the piezoelectric layer accumulates electrical charges, which are then captured by the electrodes and can be recorded as a voltage signal by a data acquisition system. This response is instantaneous, making it suitable for high-frequency or impact force sensing applications.

In this study, the newly developed MEX fabrication technique for PVDF-trFE was used to print a piezoelectric dynamic force sensor on a copper-coated Kapton substrate, as illustrated in figure 20. After the printing and curing of the PVDF-trFE, the top electrode was also printed using Novacentrix Metalon HPS-FG77 silver ink via MEX. The sensor dimensions were determined according to a commercial PVDF sensor (TE Connectivity LDT-028K) to facilitate direct comparison. Due to differences in ink properties, a 100 μm diameter nozzle was employed to print the silver electrode, and it was printed at a speed of 9 mm s^{-1}, a pressure of 68.95 kPa, and with a ΔV of 35 μm. These settings resulted in a silver electrode with a thickness of approximately 40 μm. To achieve the desired surface conductivity and film condensation, the printed silver was cured at 140 °C for 5 min, following the vendor's recommendations. This process enhanced the flexibility of the silver and prevented electrode cracking. The silver electrode was positioned at least 2 mm away from the edges of the PVDF-trFE film, ensuring uniformity in thickness, as evident from figure 15. While other electrode inks like water-based PEDOT inks are available options, the focus of this study was on well-established electrically conductive inks, given their suitability for the study objectives.

The custom-designed dynamic load frame, as depicted in figure 21, was utilized to evaluate the performance of the all-printed PVDF-trFE sensor in comparison to the commercial PVDF-trFE sensor (TE Connectivity). To generate a sinusoidal force for testing, a commercial piezoelectric stack (Physik Instrumente P-010.00H) controlled by a piezo amplifier (Physik Instrumente E-505) was employed. The dynamic

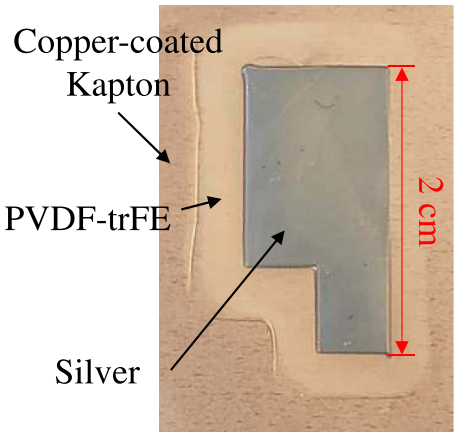

Figure 20. All printed flexible PVDF-trFE sensor for dynamic force measurement.

load applied to the sensors was accurately measured using a dynamic load cell (PCB 208C01). To ensure the proper functioning of the piezo stack, an acorn nut was used for prestressing, and this was safeguarded with a rubber sleeve. This arrangement not only protected the printed sensor from potential scratches but also served as an insulation layer. The force magnitude applied to the samples was maintained at a constant 0.5 N, and a commercial data acquisition system (Data Physics Quattro) equipped with a built-in PID controller was employed for this purpose.

The sensitivity of the sensors, defined as the voltage measured across the electrodes divided by the applied force magnitude, was assessed through a sine sweep test. The test covered a frequency range from 100 Hz to 3.2 kHz and incorporated a total of 180 logarithmically distributed frequency points.

Figure 22 displays the sensitivity of the sensors across a wide frequency spectrum. Notably, sensitivity decreases with decreasing frequency due to charge leakage effects at low frequencies. However, the sensitivity stabilizes beyond 2 kHz. In comparison, the sensitivities of the commercial PVDF sensor and the printed PVDF-trFE sensor are 0.15 V N^{-1} and 1.18 V N^{-1}, respectively. To improve sensitivity at low frequencies, the implementation of charge amplification circuits is a potential avenue for enhancement [44].

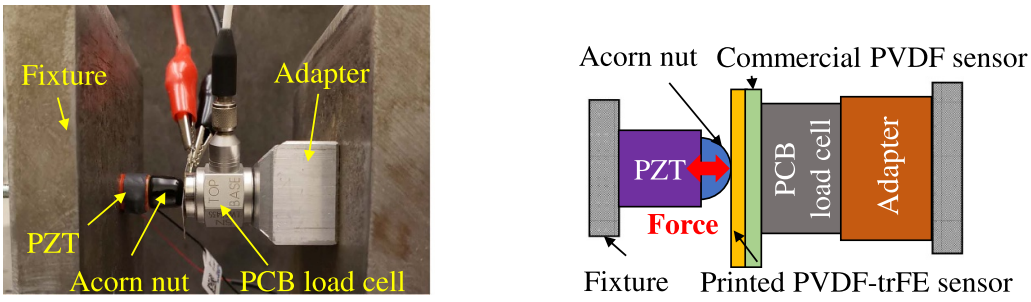

Figure 21. Customized experimental test rig for piezoelectric force sensor characterization: (a) physical assembly and (b) schematic.

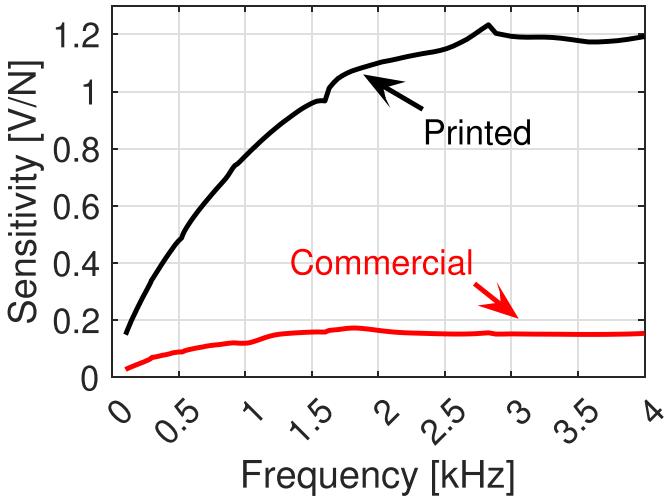

Figure 22. Sensitivity versus excitation frequency of commercial PVDF sensor and printed PVDF-trFE sensor.

6. Conclusion

This study has systematically investigated the fabrication and characterization of PVDF-trFE-based piezoelectric sensors using a novel material extrusion (MEX) approach. The key contributions of this PVDF-trFE printing approach can be succinctly summarized as follows:

- **Ink Development**—A PVDF-trFE ink formulation suitable for MEX was developed, enabling the precise deposition of PVDF-trFE films with controlled thickness and excellent uniformity. This ink consists of 2 wt.% of PVDF-trFE (20 mol.% trFE) mixed into a MEK:DMSO (1:2 volume ratio) cosolvent system.
- **Printer Tuning**—Quantitative assessments were made to understand the individual impacts of valve aperture, pressure, and printing speed on the dimensions of printed PVDF-trFE films. This led to the development and validation of a mathematical model to guide the fine-tuning of the MEX system.
- **Curing Optimization**—A comprehensive curing process including solvent drying and polymer annealing was established to achieve uniform PVDF-trFE films with robust adhesion to substrates. The optimal curing condition involves 15 min drying in a preheated mechanical oven at 90 °C, followed by annealing at 130 °C for 1 h.
- **Electric field poling**—Two distinct electric field poling methods were devised, one utilizing a silicone oil bath and the other harnessing the electric field magnification effect facilitated by a tungsten needle. The oil bath approach yielded a maximum d_{33} of 25 pC N^{-1} at an electric field of about 200 MV m^{-1} and a temperature of 60 °C for 30 min, while the tungsten needle approach achieved a maximum d_{33} of 20.5 pC N^{-1} at a poling current of about 30 μA and a temperature of 20 °C for 8 min.
- **Corona poling**—This study demonstrated the effectiveness of a corona poling setup for PVDF-trFE polarization, resulting in a d_{33} value of 20.5 pC N^{-1}, offering a promising alternative to conventional poling methods.

Building upon the well-established MEX process, this study introduced a comprehensive approach to fabricating and characterizing PVDF-trFE-based piezoelectric sensors, providing a versatile and cost-effective avenue for sensor production. This sensor was fabricated by co-printing the newly developed PVDF-trFE ink with a commercial silver ink on the same MEX system. The new sensor demonstrated significantly higher sensitivity, reaching up to 1.18 V N^{-1}, in contrast to commercial PVDF sensors, thereby rendering it well-suited for a diverse array of applications. Additionally, this sensor exhibited stable frequency responses beyond 2 kHz, further enhancing its potential in impact force sensing.

The outcomes presented herein unveil novel prospects for crafting flexible, high-performance sensors across diverse domains, such as deep space exploration, robotics, and SHM. Future research endeavors can target further optimizing the poling process, particularly focusing on the electric field magnification effect, to enable *in-situ* curing and poling of PVDF-trFE films. Further testing in simulated microgravity conditions is essential to validate the feasibility of this MEX method for in-space manufacturing. Additionally, future research should evaluate the performance of printed PVDF-trFE sensors against impacts of varying magnitudes and types, such as elastic and plastic collisions, beyond just force frequency. The incorporation of flexible, biocompatible, or transparent electrode materials is another avenue through

which this work can contribute to the burgeoning field of flexible and wearable electronics.

Data availability statement

All data that support the findings of this study are included within the article (and any supplementary files).

Acknowledgments

This research was supported by National Aeronautics and Space Administration under Award No. 80NSSC22M0172. Z D would also like to acknowledge the career development support from Institutional Development Awards (IDeA) from the National Institute of General Medical Sciences of the National Institutes of Health under Grants #P20GM103408 and P20GM109095. N M acknowledges support under the U.S. Department of Energy, Office of Nuclear Energy Advanced Sensors and Instrumentation program managed under DOE Idaho Operations Office Contract DE-AC07-05ID14517. D E acknowledges infrastructure support under DE-NE0008677 and DE-NE0008496, joint appointment support under DOE Idaho Operations Office Contract DE-AC07-05ID14517. C C acknowledges the financial support from the National Science Foundation Research Experience for Undergraduates Site: Materials for Society under Grant 1950305. Neither the U.S. Government nor any agency thereof, nor any of their employees, makes any warranty, expressed or implied, or assumes any legal liability or responsibility for the accuracy, completeness, or usefulness, of any information, apparatus, product, or process disclosed, or represents that its use would not infringe privately owned rights. References herein to any specific commercial product, process, or service by trade name, trademark, manufacturer, or otherwise, does not necessarily constitute or imply its endorsement, recommendation, or favoring by the U.S. Government or any agency. The views and opinions of authors expressed herein do not necessarily state or reflect those of the U.S. Government or any agency thereof.

ORCID iD

Zhangxian Deng https://orcid.org/0000-0003-1084-1738

References

[1] Roidev' K, Hong T, Hafermalz S, Hunkins R, Valley G and Toups L Inflatable habitat health monitoring: implementation, lessons learned, and application to lunar or Martian habitat health monitoring *AIAA SPACE 2009 Conf. & Exposition* (*September 14 2009*) p 6822 (available at: https://ntrs.nasa.gov/api/citations/20090029953/downloads/20090029953.pdf)

[2] Chandra A, Thangavelautham J and Babuscia A 2018 Modular inflatable space structures *2018 IEEE Aerospace Conf.* (IEEE) pp 1–9

[3] Litteken D, Calderon D, Gaytan C, Gov C J G, O'donnell M, Shariff K, Gov K I S, Sico M and Gov M C S Design of a microgravity hybrid inflatable airlock *2020 IEEE Aerospace Conf.* (*March 7 2020*) pp 1–17 (available at: https://ieeexplore.ieee.org/stamp/stamp.jsp?arnumber=9172313)

[4] Hughes S, Cheatwood F, Dillman R, Calomino A, Wright H, DelCorso J and Calomino A 2011 Hypersonic inflatable aerodynamic decelerator (HIAD) technology development overview *21st AIAA Aerodynamic Decelerator Systems Technology Conf. and Seminar* p 2524

[5] Seedhouse E and Seedhouse E 2015 Bigelow expandable activity module *Bigelow Aerospace: Colonizing Space one Module at a Time* (Springer) pp 87–98 (available at: https://link.springer.com/chapter/10.1007/978-3-319-05197-0_5)

[6] Munns T E *et al* 2002 Health monitoring for airframe structural characterization *NASA Technical Report* NASA/CR-2002-211428 (available at: https://ntrs.nasa.gov/api/citations/20020030899/downloads/20020030899.pdf)

[7] Litteken D A Evaluation of strain measurement devices for inflatable structures *58th AIAA/ASCE/AHS/ASC Structures, Structural Dynamics, and Materials Conf. 2017* p 0426 (available at: https://ntrs.nasa.gov/api/citations/20160014024/downloads/20160014024.pdf)

[8] Richards W L, Madaras E, Prosser W H and Studor G 2013 NASA applications of structural health monitoring technology (available at: https://ntrs.nasa.gov/search.jsp?R = 20140010525)

[9] Zhang Y, Anderson N, Bland S, Nutt S, Jursich G and Joshi S 2017 All-printed strain sensors: building blocks of the aircraft structural health monitoring system *Sens. Actuators* A **253** 165–72

[10] Zeiser R, Fellner T and Wilde J 2014 Capacitive strain gauges on flexible polymer substrates for wireless, intelligent systems *J. Sens. Sens. Syst.* **3** 77–86

[11] Hay G, Evans P, Harrison D, Southee D, Simpson G and Harrey P 2005 Characterization of lithographically printed resistive strain gauges *IEEE Sens. J.* **5** 864–71

[12] Fiorillo A S, Critello C D and Pullano S A 2018 Theory, technology and applications of piezoresistive sensors: a review *Sens. Actuators* A **281** 156–75

[13] Fujimoto K T *et al* 2020 Aerosol jet printed capacitive strain gauge for soft structural materials *npj Flex. Electron.* **4** 32

[14] Champaigne K D and Sumners J 2007 Low-power electronics for distributed impact detection and piezoelectric sensor applications *2007 IEEE Aerospace Conf.* (IEEE) pp 1–8

[15] Lin W, Wang B, Peng G, Shan Y, Hu H and Yang Z 2021 Skin-inspired piezoelectric tactile sensor array with crosstalk-free row+ column electrodes for spatiotemporally distinguishing diverse stimuli *Adv. Sci.* **8** 2002817

[16] Yu P, Liu W, Gu C, Cheng X and Fu X 2016 Flexible piezoelectric tactile sensor array for dynamic three-axis force measurement *Sensors* **16** 819

[17] Reinhardt B, Daw J and Tittmann B R 2017 Irradiation testing of piezoelectric (aluminum nitride, zinc oxide and bismuth titanate) and magnetostrictive sensors (remendur and galfenol) *IEEE Trans. Nucl. Sci.* **65** 533–8

[18] Jia N, He Q, Sun J, Xia G and Song R 2017 Crystallization behavior and electroactive properties of pvdf, P(VDF-TrFE) and their blend films *Polym. Test.* **57** 302–6

[19] McGinn C K, Kam K A, Laurila M-M, Montero K L, Mäntysalo M, Lupo D and Kymissis I 2020 Formulation, printing and poling method for piezoelectric films based on PVDF–TrFE *J. Appl. Phys.* **128** 225304

[20] Dahiya R S, Valle M, Metta G, Lorenzelli L and Pedrotti S 2008 Deposition, processing and characterization of P(VDF-TrFE) thin films for sensing applications *2008 IEEE Sensors* pp 490–3

[21] Cho Y, Park J B, Kim B-S, Lee J, Hong W-K, Park I-K, Jang J E, Sohn J I, Cha S and Kim J M 2015 Enhanced energy harvesting based on surface morphology engineering of P(VDF-TrFE) film *Nano Energy* **16** 524–32

[22] Mokhtari F, Azimi B, Salehi M, Hashemikia S and Danti S 2021 Recent advances of polymer-based piezoelectric composites for biomedical applications *J. Mech. Behav. Biomed. Mater.* **122** 104669
[23] Eltouby P, Shyha I, Li C and Khaliq J 2021 Factors affecting the piezoelectric performance of ceramic-polymer composites: a comprehensive review *Ceram. Int.* **47** 17813–25
[24] Jain A, Prashanth K J, Sharma A K, Jain A and Rashmi P N 2015 Dielectric and piezoelectric properties of PVDF/PZT composites: a review *Polym. Eng. Sci.* **55** 1589–616
[25] Haque R I, Vié R, Germainy M, Valbin L, Benaben P and Boddaert X 2015 Inkjet printing of high molecular weight PVDF-TrFE for flexible electronics *Flex. Print. Electron.* **1** 015001
[26] Thuau D, Kallitsis K, Santos F D D and Hadziioannou G 2017 All inkjet-printed piezoelectric electronic devices: energy generators, sensors and actuators *J. Mater. Chem.* **5** 9963–6
[27] Marandi M and Tarbutton J 2019 Additive manufacturing of single- and double-layer piezoelectric PVDF-TrFE copolymer sensors *Proc. Manuf.* **34** 666–71
[28] Porter D A, Hoang T V T and Berfield T A 2017 Effects of *in-situ* poling and process parameters on fused filament fabrication printed PVDF sheet mechanical and electrical properties *Addit. Manuf.* **13** 81–92
[29] Beringer L T, Xu X, Shih W, Shih W-H, Habas R and Schauer C L 2015 An electrospun PVDF-TrFe fiber sensor platform for biological applications *Sens. Actuators* A **222** 293–300
[30] Abolhasani M M, Shirvanimoghaddam K, Khayyam H, Moosavi S M, Zohdi N and Naebe M 2018 Towards predicting the piezoelectricity and physiochemical properties of the electrospun P(VDF-TrFE) nanogenrators using an artificial neural network *Polym. Test.* **66** 178–88
[31] Banquart A, Callé S, Levassort F, Fritsch L, Ossant F, Siewe S T, Chevalliot S, Capri A and Grégoire J-M 2021 Piezoelectric P(VDF-TrFE) film inkjet printed on silicon for high-frequency ultrasound applications *J. Appl. Phys.* **129** 195107
[32] Closson A, Richards H, Xu Z, Jin C, Dong L and Zhang J X J 2021 Method for inkjet-printing PEDOT:PSS polymer electrode arrays on piezoelectric PVDF-TrFE fibers *IEEE Sens. J.* **21** 26277–85
[33] Deng Z, Rosales B, Choi L, Mooers S and Johnson B C 2020 3D-printed and wireless piezoelectric tactile sensors *Proc. SPIE* **11375** 269–75
[34] Rich B 3D printer for human tissue now available for research onboard the ISS National Laboratory (available at: https://www.issnationallab.org/3d-printer-for-human-tissue-now-available-for-research-onboard-the-iss-national-laboratory/)
[35] Li W, Lan D and Wang Y 2020 Exploration of direct-ink-write 3d printing in space: droplet dynamics and patterns formation in microgravity *Microgravity Sci. Technol.* **32** 935–40
[36] Van Ombergen A *et al* 2023 3d bioprinting in microgravity: opportunities, challenges and possible applications in space *Adv. Healthcare Mater.* **12** 2300443
[37] Cordonier G J *et al* 2021 Direct foam writing in microgravity *npj Microgravity* **7** 55
[38] Piezotech P(VDF-TrFE) 70/30, 75/25, or 80/20 mol Copolymer Resin 10 gram (available at: https://piezopvdf.com/piezotech-PVDF-TrFE-resin-10-gram/)
[39] White A, McKibben N and Deng Z 2022 Additive manufacturing of piezoelectric force sensors *Proc. SPIE* **12042** 342–9
[40] Ikei A, Wissman J, Sampath K, Yesner G and Qadri S N 2021 Tunable *in situ* 3D-printed PVDF-TrFE piezoelectric arrays *Sensors* **21** 5032
[41] Li Y, Feng W, Meng L, Tse K M, Li Z, Huang L, Su Z and Guo S 2021 Investigation on *in-situ* sprayed, annealed and corona poled PVDF-TrFE coatings for guided wave-based structural health monitoring: from crystallization to piezoelectricity *Mater. Des.* **199** 109415
[42] Kim H, Torres F, Wu Y, Villagran D, Lin Y and Tseng T-L 2017 Integrated 3D printing and corona poling process of PVDF piezoelectric films for pressure sensor application *Smart Mater. Struct.* **26** 085027
[43] Ducrot P-H, Dufour I and Ayela C 2016 Optimization of PVDF-TrFE processing conditions for the fabrication of organic MEMS resonators *Sci. Rep.* **6** 19426
[44] Ramanathan A K, Headings L M and Dapino M J 2018 Near DC force measurement using PVDF sensors *Proc. SPIE* **10602** 88–100